INTERNATIONAL JOURNAL FOR NUMERICAL METHODS IN FLUIDS
Int. J. Numer. Meth. Fluids 2007; **53**:1707–1726
Published online 10 October 2006 in Wiley InterScience (www.interscience.wiley.com). DOI: 10.1002/fld.1380

Hybrid lattice Boltzmann finite-difference simulation of axisymmetric swirling and rotating flows

Haibo Huang*,†, T. S. Lee and C. Shu

Fluid Division, Department of Mechanical Engineering, National University of Singapore, 10 Kent Ridge Crescent, Singapore 119260, Singapore

SUMMARY

The axisymmetric flows with swirl or rotation were solved by a hybrid scheme with lattice Boltzmann method for the axial and radial velocities and finite-difference method for the azimuthal (or swirl) velocity and the temperature. An incompressible axisymmetric lattice Boltzmann D2Q9 model was proposed to solve the axial and radial velocities through inserting source terms into the two-dimensional lattice Boltzmann equation. Present hybrid scheme was firstly validated by simulations of Taylor–Couette flows between two concentric cylinders. Then the benchmark problems of melt flow in Czochralski crystal growth were studied and accurate results were obtained. Numerical experiment demonstrated that present axisymmetric D2Q9 model is more stable than the previous axisymmetric D2Q9 model (*J. Comp. Phys.* 2003; **186**(1):295–307). Hence, compared with the previous model, present numerical method provides a significant advantage in simulation melt flow cases with high Reynolds number and high Grashof number.

Received 3 June 2006; Revised 24 August 2006; Accepted 25 August 2006

KEY WORDS: lattice Boltzmann; axisymmetric; source term; Taylor–Couette flow; crystal growth

1. INTRODUCTION

Many important engineering flows involve swirl or rotation, for example, the flows in combustion, turbomachinery and mixing tanks. Here, we are interested in the axisymmetric flows with swirl and rotation. Since the gradient for any variable in the azimuthal direction is zero, an axisymmetric swirling flow is a quasi-three-dimensional (3D) problem for conventional Navier–Stokes (NS) solvers in the cylindrical coordinate system. In this paper two typical axisymmetric swirling and rotating flows would be studied.

*Correspondence to: Haibo Huang, Fluid Division, Department of Mechanical Engineering, National University of Singapore, 10 Kent Ridge Crescent, Singapore 119260, Singapore.
†E-mail: g0301108@nus.edu.sg

One is Taylor–Couette flow between two concentric cylinders. At low rotational speed of the inner cylinder, the flow is steady and the vortices are planar. Three-dimensional vortices would begin to appear when the speed of rotation exceeds a critical value that depends on the ratio of radius of two cylinders. Previously, there are some studies on Taylor–Couette flow using the conventional NS solvers [1].

The other typical axisymmetric swirling flow is the melt flow in Czochralski (CZ) crystal growth. CZ crystal growth is one of the major prototypical systems for melt-crystal growth. It has received the most attention because it can provide large single crystals. In typical CZ crystal growth systems, the high Reynolds number and Grashof number of the melt make numerical simulation difficult. The conventional CFD methods such as finite volume and finite-difference methods have been developed to simulate the CZ crystal growth flow problems [2–4]. The second-order central difference scheme is usually chosen to discretize the convection terms in NS equations. However, for melt flows with high Reynolds number and Grashof number which are the requirement of growth of larger and perfect crystals, the convection terms in the NS equations become dominant and the second-order central difference scheme may be unsuitable due to enhanced numerical instability [3]. However, if the low-order upwind scheme is applied, we can only obtain accurate solutions by using very fine grid [3]. Considering the discretization problem in conventional CFD method, lattice Boltzmann method (LBM) was proposed to simulate the melt flow in CZ crystal flow [5].

It is well known that LBM has been proposed as an alternative numerical scheme for solving the incompressible NS equations [6, 7] and have proven to be superior in accuracy and efficiency for certain applications. One main advantage is that the convection operator of LBM in phase space is linear which may overcome the above discretization problem in conventional CFD method.

Since the standard two-dimensional (2D) LBM is based on the Cartesian coordinate system, the axisymmetric swirling flows cannot be simulated as a quasi-3D problem in cylindrical coordinates using standard 2D LBM. On the other hand, of course, the axisymmetric swirling flows can be solved by the 3D LBM [8, 9] which using the 3D cubic lattices with proper curved wall boundary treatment directly. However, that means a large grid size. It is not efficient to simulate an axisymmetric swirling flow problem in that way.

To simulate the axisymmetric flows without rotation more efficiently, in 2001, Halliday *et al*. [10] proposed an axisymmetric D2Q9 model and it seems very successful for simulation steady flow in straight tube. The main idea of the model is inserting several spatial and velocity-dependent 'source' terms into the 2D lattice Boltzmann equation (LBE).

Following the idea of Halliday *et al*. [10], Peng *et al*. [5] used LBM to study the melt flow in CZ crystal growth as a quasi-3D problem. They proposed an axisymmetric D2Q9 LBM to solve the axial and radial velocity in an axisymmetric plane and swirl velocity and temperature were solved by finite-difference method. However, Peng *et al*. [5] only simulated test cases of lower Reynolds number and Grashof number.

It was found that the axisymmetric model proposed by Peng *et al*. [5] is unstable for simulations of melt flows with high Reynolds number ($Re = 10^4$) and high Grashof number ($Gr = 10^6$) even with very fine grid such as 200×200.

On the other hand, since the model proposed by Peng *et al*. is derived from the standard D2Q9 model, the compressible effect of standard D2Q9 model [11, 12] may be involved in their simulation.

To improve the numerical stability and eliminate the compressibility effect of standard LBM, here a new incompressible axisymmetric D2Q9 model was proposed. This axisymmetric D2Q9 model was derived from the incompressible D2Q9 model proposed by He and Luo [12].

DOI: 10.1002/fld

In this paper, the axisymmetric swirling flows would be solved by a hybrid scheme. The axial and radial velocities were solved by LBM and swirl velocity and temperature were solved by finite-difference method. This hybrid scheme was firstly validated by simulation of Taylor–Couette flows between two concentric cylinders. Then the melt flows in CZ crystal growth were studied in detail. Our numerical results were compared with available data of Raspo *et al*. [4] and Xu *et al*. [3]. Through numerical tests, present axisymmetric D2Q9 model was proved more stable than the model of Peng *et al*. [5] for steady axisymmetric swirling and rotating flows. As a result, our hybrid scheme can give accurate results for melt flow with high Reynolds number and high Grashof number using smaller grid size.

2. NUMERICAL METHODS

We consider the problems of the laminar axisymmetric swirling flow of an incompressible liquid with an axis in x direction. The following continuity equation (1) and NS momentum equations (2) in the pseudo-Cartesian coordinates (x, r) are used to describe the flow in axial and radial directions

$$\partial_\beta u_\beta = -\frac{u_r}{r} \tag{1}$$

$$\partial_t u_\alpha + \partial_\beta(u_\beta u_\alpha) + \frac{1}{\rho_0}\partial_\alpha p - \nu\partial_\beta(\partial_\beta u_\alpha) = -\frac{u_\alpha u_r}{r} + \frac{\nu}{r}\left(\partial_r u_\alpha - \frac{u_r}{r}\delta_{\alpha r}\right) + \frac{u_z^2}{r}\delta_{\alpha r} + S \tag{2}$$

where u_β $(\beta = x, r)$ is the two components of velocity and u_α is the velocity u_x or u_r. S is the additional source term that may appear in some flow problems. In the above equations we adopt the Einstein summation convention.

For the axisymmetric swirling flow, there are no circumferential gradients but there may still be non-zero swirl velocities u_z. The momentum equation of azimuthal velocity is

$$\frac{\partial u_z}{\partial t} + u_x\frac{\partial u_z}{\partial x} + u_r\frac{\partial u_z}{\partial r} = \nu\left(\frac{\partial^2 u_z}{\partial x^2} + \frac{\partial^2 u_z}{\partial r^2}\right) + \frac{\nu}{r}\left(\frac{\partial u_z}{\partial r} - \frac{u_z}{r}\right) - \frac{u_r u_z}{r} \tag{3}$$

Here we proposed an axisymmetric lattice Boltzmann D2Q9 model to recover above equations (1) and (2) through the Chapman–Enskog expansion (refer to Appendix A). Since the lattice Bhatnagar–Gross–Krook (LBGK) model is the simplest model among the LBE models in application, our axisymmetric lattice Boltzmann model is derived from an incompressible LBGK D2Q9 model [12]. The nine discrete velocities of our model are as follows:

$$\mathbf{e}_i = \begin{cases} (0, 0), & i = 0 \\ (\cos[(i-1)\pi/2], \sin[(i-1)\pi/2])c, & i = 1, 2, 3, 4 \\ \sqrt{2}(\cos[(i-5)\pi/2 + \pi/4], \sin[(i-5)\pi/2 + \pi/4])c, & i = 5, 6, 7, 8 \end{cases} \tag{4}$$

where $c = \delta_x/\delta_t$, and in our studies $c = 1$. δ_x and δ_t are the lattice spacing and time step size.

The evaluation equation to describe 2D flow in (x, r) pseudo-Cartesian coordinates is illustrated as Equation (5) which is similar to the evaluation equation for standard D2Q9 model in 2D (x, y)

DOI: 10.1002/fld

Cartesian coordinates. The difference is that a source term $h_i(x, r, t)$ was incorporated into the microscopic evaluation equation

$$f_i(x + ce_{ix}\delta_t, r + ce_{ir}\delta_t, t + \delta_t) - f_i(x, r, t) = \frac{1}{\tau}[f_i^{\mathrm{eq}}(x, r, t) - f_i(x, r, t)] + h_i(x, r, t) \quad (5)$$

In Equation (5), $f_i(x, r, t)$ is the distribution function for particles with velocity $\mathbf{e}_i$ at position (x, r) and time t. τ is the relax time constant. The relax time constant τ and the fluid viscosity satisfies equation

$$v = c_s^2 \delta_t (\tau - 0.5) \quad (6)$$

where $c_s = c/\sqrt{3}$. In Equation (5), the equilibrium distribution f_i^{eq} of incompressible D2Q9 model [12] is defined as

$$f_i^{\mathrm{eq}}(x, r, t) = \omega_i \frac{p}{c_s^2} + \omega_i \rho_0 \left[\frac{\mathbf{e}_i \cdot \mathbf{u}}{c_s^2} + \frac{(\mathbf{e}_i \cdot \mathbf{u})^2}{2c_s^4} - \frac{\mathbf{u}^2}{2c_s^2} \right], \quad i = 0, 1, 2, \ldots, 8 \quad (7)$$

where p is the pressure and ρ_0 is the density of fluid. In the above expressions, for D2Q9 model, $\omega_0 = \frac{4}{9}$, $\omega_i = \frac{1}{9}$ $(i = 1, 2, 3, 4)$, $\omega_i = \frac{1}{36}$ $(i = 5, 6, 7, 8)$. It is noticed that the main difference between above incompressible D2Q9 model and the standard D2Q9 model is the form of Equation (5).

3. HYBRID SCHEME

3.1. Implementation of the axisymmetric model and finite difference

In numerical simulations, one must ensure that the Mach number is low and the density fluctuation $(\delta\rho)$ is of order $O(M^2)$ [12]. The additional limit $L_x/(c_s T) \ll 1$ is illustrated in our derivation (refer to Appendix A). In this part, we mainly discuss the implementation of the axisymmetric D2Q9 model.

In the D2Q9 model, $f_i(x, r, t)$ is the distribution function. The macroscopic pressure p and momentum $\rho_0 \mathbf{u}$ are defined as

$$\sum_{i=0}^{8} f_i = p/c_s^2, \quad \sum_{i=0}^{8} f_i e_{i\alpha} = \rho_0 u_\alpha \quad (8)$$

The two main steps of lattice BGK model are collision and streaming. In the collision step, a group of calculations (9) and (10) are implemented

$$f_i^{\mathrm{ne}} = f_i(x, r, t) - f_i^{\mathrm{eq}}(x, r, t) \quad (9)$$

$$f_i^{+}(x, r, t) = f_i^{\mathrm{eq}}(x, r, t) + \left(1 - \frac{1}{\tau}\right) f_i^{\mathrm{ne}} + \delta_t h_i^{(1)} + \delta_t^2 h_i^{(2)} \quad (10)$$

where f_i^{eq} is the equilibrium momentum distribution function which can be obtained through Equation (7), f_i^{ne} is the non-equilibrium part of distribution function, $h_i^{(1)}$ and $h_i^{(2)}$ are the 'source' terms added into the collision step, which can calculated through Equations (A11) and (A23),

DOI: 10.1002/fld

respectively (refer to Appendix A). For simplicity, in our study, $\delta_t = \delta_x \cdot f_i^+$ is the post-collision distribution function.

In the streaming step, the new distribution function value obtained from Equation (10) would propagate to neighbouring eight lattices. That procedure can be represented as follows:

$$f_i(x + e_{ix}\delta_t, r + e_{ir}\delta_t, t + \delta_t) = f_i^+(x, r, t) \tag{11}$$

For the velocity derivations in Equation (A23), the terms $\partial_r u_x + \partial_x u_r$, $\partial_x u_x$ and $\partial_r u_r$ can all be obtained through Equation (12) with $\alpha = x$, $\beta = r$; $\alpha = \beta = x$ and $\alpha = \beta = r$, respectively

$$\rho_0 \nu(\partial_\beta u_\alpha + \partial_\alpha u_\beta) = -\left(1 - \frac{1}{2\tau}\right) \sum_{i=0}^{8} f_i^{(1)} e_{i\alpha} e_{i\beta} = -\left(1 - \frac{1}{2\tau}\right) \sum_{i=0}^{8} f_i^{\mathrm{ne}} e_{i\alpha} e_{i\beta} + o(\varepsilon^2) \tag{12}$$

For the term $\partial_r u_x$ in Equation (A23), it is equal to $(\partial_r u_x + \partial_x u_r) - \partial_x u_r$. Since $(\partial_r u_x + \partial_x u_r)$ can be easily obtained by Equation (12), only value of $\partial_x u_r$ is left unknown to determine $\partial_r u_x$. Here finite-difference method is used to obtain $\partial_x u_r$ at lattice node (i, j), which can be calculated by

$$(\partial_x u_r)_{i,j} = ((u_r)_{i+1,j} - (u_r)_{i-1,j})/(2\delta_x) \tag{13}$$

The values of $\partial_r u_x + \partial_x u_r$, $\partial_x u_x$, $\partial_r u_r$, $\partial_r u_x$ and $\partial_x u_r$ for the lattice nodes which just on the wall boundary can also be calculated from Equations (12) and (13). Hence, for the additional source term in our model, most velocity gradient terms can be obtained from high-order momentum of distribution function, which is consistent with the philosophy of the LBM.

For the momentum equation of azimuthal velocity, it was solved by finite-difference method. Equation (3) can be solved explicitly by using first-order forward difference scheme in time and the second-order central difference scheme (e.g. Equations (15) and (16)) for space discretization as follows:

$$u_z^{n+1} = u_z^n + \delta_t \left[-\left(u_x^n \frac{\partial u_z^n}{\partial x} + u_r^n \frac{\partial u_z^n}{\partial r} \right) + \nu \left(\frac{\partial^2 u_z^n}{\partial x^2} + \frac{\partial^2 u_z^n}{\partial r^2} \right) + \frac{\nu}{r} \left(\frac{\partial u_z^n}{\partial r} - \frac{u_z^n}{r} \right) - \frac{u_r^n u_z^n}{r} \right] \tag{14}$$

$$\frac{\partial u_z^n}{\partial x} = \frac{(u_z^n)_{i+1,j} - (u_z^n)_{i-1,j}}{2\delta_x} \tag{15}$$

$$\frac{\partial^2 u_z^n}{\partial x^2} = \frac{(u_z^n)_{i+1,j} + (u_z^n)_{i-1,j} - 2(u_z^n)_{i,j}}{\delta_x^2} \tag{16}$$

3.2. Boundary condition

Boundary condition is an important issue when using LBM to simulate the fluid flows [13]. It is well known that bounce back scheme is one of the simplest schemes in LBM. Here this scheme was applied for non-slip wall boundary condition.

For the axisymmetric boundary condition (i.e. the x-axis), the specular reflection scheme was applied to lattice nodes in axis [5]. As we know, specular reflection scheme can be applied to free-slip boundary condition where no momentum is to be exchanged with the boundary along the tangential component. Hence, for the free surface (e.g. $x = H$, $R_x < r < R_c$ in Figure 4) in our simulated case, the specular boundary condition is also applied.

DOI: 10.1002/fld

When using the finite-difference method to solve the equation for swirl velocity or the heat equation, we may encounter the Neumann boundary condition. Here the Neumann boundary condition was transferred into the Dirichlet boundary condition. For example, if $\partial T/\partial x = 0$ was imposed in the boundary $x = 0$ (i.e. the r-axis, refer to Figure 4), the T value in the boundary lattice node $(1, j)$ can be determined by extrapolation from the inner lattice nodes as $(T)_{1,j} = (4(T)_{2,j} - (T)_{3,j})/3$, where j is the lattice index in r coordinate.

4. RESULTS AND DISCUSSION

4.1. Taylor–Couette flows

Figure 1 illustrates the geometry of Taylor–Couette flow, our computational domain is a r–x plane. The governing equations for the axisymmetric swirl flow are Equations (1)–(3) with $S = 0$ in Equation (2). The boundary conditions used in our simulation are also illustrated in Figure 1. The Reynolds number is defined as $Re = WD/v$, where W is the azimuthal velocity of inner cylinder, D is the gap of the annulus and v is the fluid viscosity. The radius ratio of inner cylinder and out cylinder is set as 0.5. The aspect ratio is set as 3.8.

Firstly, the grid independence of the results was examined and it was found that with 20×76 uniform grid, present numerical method can give out very accurate results. The maximum stream function values in r–x plane for cases of $Re = 85$, 100 and 150 are listed in Table I. It seems that even with grid 20×76, the results of our hybrid scheme agree well with those of Liu [1] which were obtained by very fine grid. The contours of stream function, pressure and vorticity for case $Re = 150$ are illustrated in Figure 2. From Figure 2, we can see the four cell secondary modes. These contours and flow pattern also agree well with results of Liu [1].

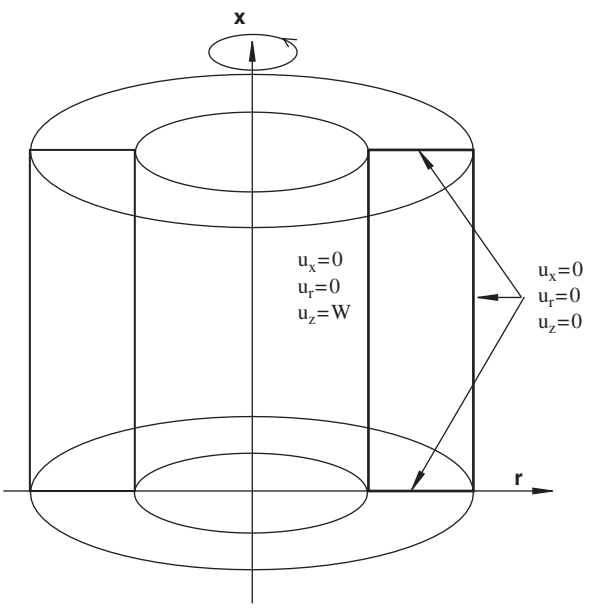

Figure 1. Geometry of Taylor–Couette flow and boundary conditions.

DOI: 10.1002/fld

Table I. The maximum stream function value in x–r plane for Taylor–Couette flow (grid 20×76).

Re	$\psi_{\max}$	$\psi_{\max}$ [1]
85	4.810×10^{-2}	4.854×10^{-2}
100	5.501×10^{-2}	5.542×10^{-2}
150	6.427×10^{-2}	6.439×10^{-2}

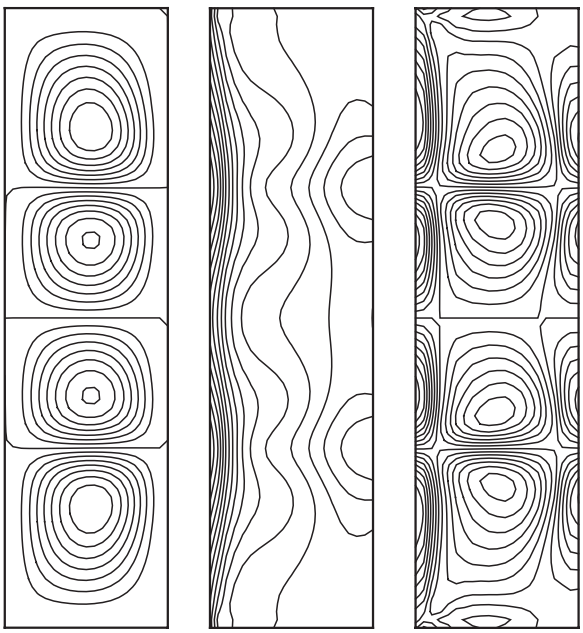

Figure 2. The contour of stream function, pressure and vorticity for case $Re = 150$ with grid 20×76.

Secondly, the efficiency of our hybrid scheme (LBM + FD) and explicit finite volume method (FVM) was compared. The efficiency is evaluated by comparing the respective computing times required. To minimize the influence of computers and convergence criterion, in this study, both our LBM+FD solver and FVM solver (FLUENT) were executed on a super computer (Compaq ES40: total performance of 5300 Mflops) in the National University of Singapore. In our simulations, the zero velocities were initialized everywhere. The residual used to monitor the convergence is defined using the u_z-momentum equation for two solvers as follows:

$$\text{LBM} + \text{FD}: \ \sum \left| \frac{u_z^{n+1} - u_z^n}{\delta t} \right| \tag{17}$$

$$\text{FVM}: \ \sum \left| \frac{\partial u_z^n}{\partial t} + u_x^n \frac{\partial u_z^n}{\partial x} + u_r^n \frac{\partial u_z^n}{\partial r} + \frac{u_r^n u_z^n}{r} - \nu \left(\frac{\partial^2 u_z^n}{\partial x^2} + \frac{\partial^2 u_z^n}{\partial r^2} \right) - \frac{\nu}{r} \left(\frac{\partial u_z^n}{\partial r} - \frac{u_z^n}{r} \right) \right| \tag{18}$$

DOI: 10.1002/fld

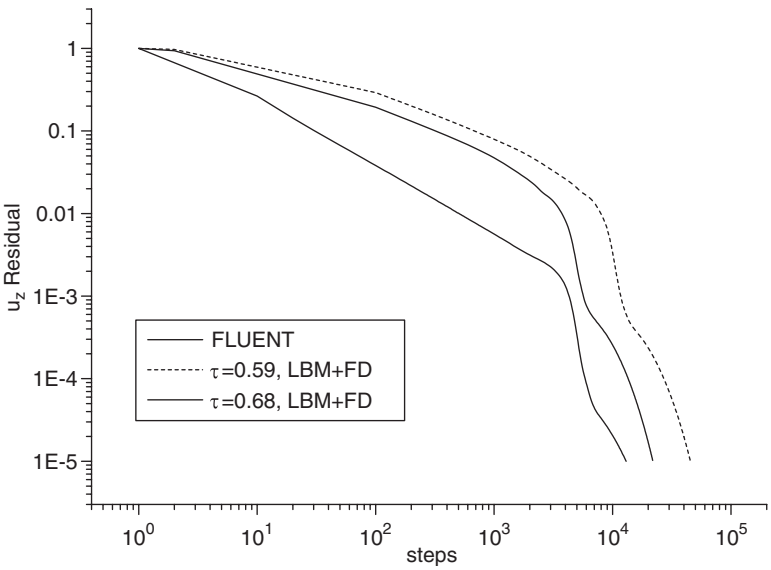

Figure 3. Convergence history for FLUENT and the hybrid scheme (LBM + FD).

Table II. Comparison of CPU time for hybrid scheme and FVM simulation of Taylor–Couette flow ($Re = 100$, grid 30×114).

	Steps	CPU time (s)	$\psi_{\max}$
FLUENT	13 200	1523	5.530×10^{-2}
LBM + FD ($\tau = 0.59$)	45 300	1560	5.553×10^{-2}
LBM + FD ($\tau = 0.68$)	21 800	742	5.612×10^{-2}
Liu	—	—	5.542×10^{-2}

Note that all the computations are carried out on a single-CPU of the computer Compaq ES40, which does not take parallel advantage of the LBM.

For comparison purpose, the case of Taylor–Couette flow for $Re = 100$ using grid 30×114 was simulated. In the explicit FVM solver (FLUENT), the courant number was set as CFL = 1. The convergence for the hybrid scheme and FVM solver is displayed in Figure 3 in terms of relative residual error (the residual expressions were normalized by the initial residual). The overall convergence trend of our hybrid scheme is similar to that of FVM solver.

The CPU times for hybrid scheme and FVM are also listed in Table II. It seems that to reach the same convergence criterion, our LBM + FD solver ($\tau = 0.59$) takes almost same CPU time as the explicit FVM solver. The calculation of LBM + FD solver with relax time constant $\tau = 0.68$ is faster than calculation with $\tau = 0.59$.

According to our experience, for a 2D flow case with same grid, usually the explicit FLUENT solver requires about eight times larger CPU time per iteration than our 2D LBM solver. It is also observed that for axisymmetric cases without rotation, the FLUENT solver requires about four

DOI: 10.1002/fld

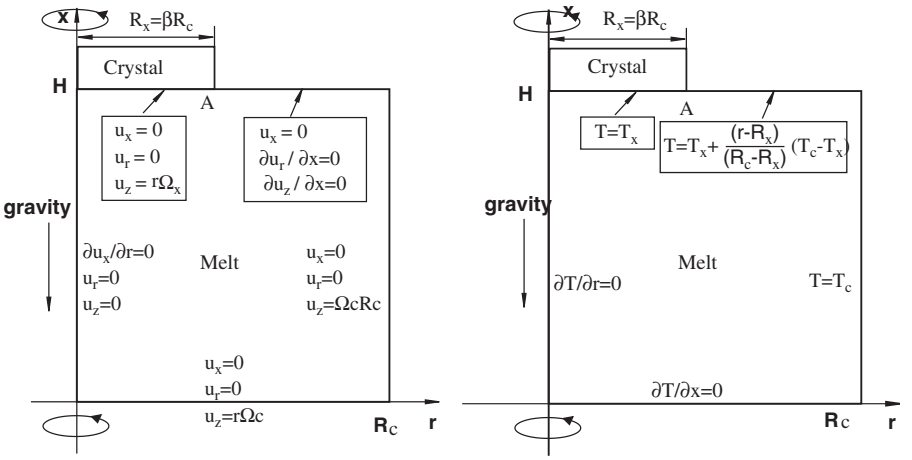

Figure 4. The momentum and thermal boundary conditions of melt flow in Czochralski crystal growth.

times larger CPU time per iteration than axisymmetric LBM. That may be due to the fact that compared with a 2D case, FLUENT almost does not require more CPU time for axisymmetric case while axisymmetric LBM need more effort to calculate the source terms.

From Table II, it is found that for the axisymmetric flow with rotation, compared with LBM+FD solver, FLUENT requires about 3.35 times larger CPU time per iteration. It is also observed from our numerical experiment that the time spent for the solving of Equation (14) (i.e. FD) in our LBM + FD scheme is around 12% of total CPU time.

4.2. Melt flows in CZ crystal growth

In the CZ crystal growth, the melt flow is very complex because it is a combination of natural convection due to thermal gradients and forced convection due to rotation of the crystal and the crucible. Here, the Wheeler benchmark problem [14] in CZ crystal growth is taken as the test example to validate our numerical method. The configuration and the momentum and thermal boundary conditions are all illustrated in Figure 4. In the problem, a vertical cylindrical crucible filled with a melt to a height $H = R_c$ rotates with an angular velocity Ω_c. In the top of the melt, it is bounded by a coaxial crystal with radius $R_x = \beta R_c$ ($\beta = 0.4$) which rotates with angular velocity Ω_x. There is a phase boundary between the crystal and melt. In the top right part of melt ($R > R_x$), there is a free surface. The u_x, u_r, u_z are the axial, radial and azimuthal velocity components, respectively.

The continuity and momentum equations for CZ crystal growth can also illustrated by Equations (1)–(3). In Equation (2), since the Boussinesq approximation is applied to this buoyancy force term, $S = g\beta_0(T - T_c)\delta_{\alpha x}$, where g is the acceleration due to gravity, β_0 is the thermal expansion coefficient, T_c is the temperature of crucible. The governing equation of temperature is

$$\frac{\partial T}{\partial t} + u_x \frac{\partial T}{\partial x} + u_r \frac{\partial T}{\partial r} = \frac{v}{Pr}\left(\frac{\partial^2 T}{\partial x^2} + \frac{\partial^2 T}{\partial r^2} + \frac{1}{r}\frac{\partial T}{\partial r}\right) \tag{19}$$

DOI: 10.1002/fld

This equation can be solved explicitly by finite-difference method as Equation (14). However, in this part, to accelerate convergence rate, finite-difference equations for Equations (3) and (19) were solved by the tridiagonal matrix algorithm (TDMA) at each iteration.

The dimensionless parameters: Reynolds number Re_c, Re_x, Prandtl number Pr and Grashof number Gr are defined as

$$Re_c = \frac{R_c^2 \Omega_c}{\nu}, \quad Re_x = \frac{R_c^2 \Omega_x}{\nu}, \quad Pr = \frac{\nu}{\alpha}, \quad Gr = \frac{g\beta_0 (T_c - T_x) R_c^3}{\nu^2}$$

where α is the thermal diffusivity. In our simulations, $Pr = 0.05$. The value of characteristic velocity $U_t = \sqrt{\beta_0 g (T_c - T_x) R_c}$ was chosen as 0.15 for $Gr \leqslant 10^5$ and 0.25 for $Gr > 10^5$. When U_t is determined, the kinetic viscosity ν can be determined by Gr. And then the relaxation times τ is determined by Equation (6). Another characteristic velocity $U_h = R_c \Omega_x \beta$ is also used when $Gr = 0$ in our simulation and it is usually set as 0.1.

For the results, R_c and ν / R_c are used as the characteristic length, speed scales. The dimensionless temperature is defined as $T' = (T - T_x)/(T_c - T_x)$, where T_x is the temperature of the crystal.

In our simulations, the zero velocities and zero temperature were initialized everywhere and the convergence criterion in our simulation is set as

$$\sum_{i,j} \frac{\| \sqrt{[u_x(x_i, r_j, t + \delta_t) - u_x(x_i, r_j, t)]^2 + [u_r(x_i, r_j, t + \delta_t) - u_r(x_i, r_j, t)]^2} \|}{\| \sqrt{[u_x(x_i, r_j, t + \delta_t)]^2 + [u_r(x_i, r_j, t + \delta_t)]^2} \|} < 10^{-6} \tag{20}$$

where i, j are the lattice nodes index.

To compare with available data of Raspo *et al*. [4], Buckle *et al*. [2] and Xu *et al*. [3], all of the present numerical results are expressed as stream function. The stream function ψ is defined as

$$\frac{\partial \psi}{\partial r} = -r u_x, \quad \frac{\partial \psi}{\partial x} = -r u_r \tag{21}$$

with $\psi = 0$ on all the boundaries of computing plane. In the following, the minimum and maximum values of stream function denoted by $\psi_{\min}$ and $\psi_{\max}$ will be used to compare the results of our hybrid scheme with available data in the literature [3, 4].

Firstly, the grid independence of the results was examined. Case A2, with $Gr = 0$, $Re_x = 10^3$, $Re_c = 0$, was calculated using three grids. The $\psi_{\min}$ and $\psi_{\max}$ are compared with the result of

Table III. Grid independence test for case A2, $Gr = 0$, $Re_x = 10^3$, $Re_c = 0$.

Grid	$\psi_{\min}$	$\psi_{\max}$
50×50	-4.73	1.80×10^{-4}
100×100	-4.98	7.31×10^{-5}
150×150	-5.046	6.52×10^{-5}
Reference [4]	-5.074	7.89×10^{-5}

DOI: 10.1002/fld

Raspo *et al*. [4] in Table III, where we can see that an 100×100 grid is sufficient to obtain accurate results.

Secondly, as many as 11 cases with difference parameter sets were simulated. The 11 cases were classified into four groups. In group A, the crystal rotate with Re_x varying from 10^2 to 10^4, while the crucible is at rest and Gr is set to zero. In group B, the crystal and crucible rotate in opposite directions. Group A and B are all forced convection problems. Cases in group C are natural convection problems. Cases in group D are more like practical applications because these melt flows combined both the natural convection and forced convection were investigated.

Table IV shows the comparison of computed minimum and maximum stream function for all the above 11 cases. In the table, the number in the bracket followed the case type indicates the grid size used. If not specified, the grid used in our simulation is 100×100. For comparison, we also present the results of Xu *et al*. [3] using the second-order difference scheme with a grid size of 80×80. In all cases, the maximum absolute values of stream function computed by the LBM agree very well with those of Xu *et al*. [3]. Some very small deviations between the computed minimum absolute values of stream function can be neglected since the minimum absolute values of stream function are so small compared with the maximum absolute values. Due to numerical stability, the simulation of cases A3, B3, C2 used fine grids. The issue of numerical stability will be discussed in detail in Section 4.3.

Figure 5 shows the calculated streamlines and temperature contours of case A2. That is a typical result for group A. There is a primary vortex induced by rotation of the crystal. For the cases of group A, when the Reynolds number of crystal rotation is increased from 10^2 to 10^4, the maximum absolute value of the stream function increases from 0.2272 to 40.47, which means the intensity of vortex increases. For higher Reynolds number cases in group A, the centre of the vortex moves towards the side wall of the crucible and the highest velocity region moves from the upper left corner to the upper right corner. Hence, better quality crystal can be produced if Re_x is high.

Figure 6 illustrates the streamlines and temperature contours of case B2, which represent the flow pattern of group B. For cases in group B, the crystal and crucible rotate in opposite directions. As a result, there are two vortices with opposite directions appearing in the upper left corner just below the crystal and the lower right corner. With the increase in rotation speeds of the crystal and crucible, the upper left vortex produced moves towards right corner and the lower right primary vortex induced by the crucible rotation moves to the left and dominates the flow field. It is noticed that for cases of forced convection problems where $Gr = 0$ (cases in group A and B), the contours of temperature are very similar.

Figure 7 shows the streamlines and temperature contours of case C2. In this natural convection flow case, the crucible and the crystal are all at rest. There is a primary vortex induced by the temperature difference between the crystal and crucible. Compared with temperature contours in Figures 5 and 6, the temperature contours of case C2 in Figure 7 shows the effect of buoyancy force on the temperature field.

Figure 8 shows the streamlines and temperature contours of case D2. The streamlines and contours illustrated the combined effects of the natural convective flow and forced convective flow. It is found that the streamlines and temperature contours of cases in group D are very similar to those of case C1 whose Grashof number is also equal to 10^5. From Table IV, it is also found that the $\psi_{\max}$ of cases in group D are all very close to that of case C1. That means in cases of group D, if $Re_x < 10^3$, the natural convective flow dominates the melt flow while the force convective flow induced by the crystal only has minor effect.

DOI: 10.1002/fld

Table IV. Some results for the test cases by the hybrid scheme and QUICK [3].

Case	Gr	Re_x	Re_c	ψ_{min}	ψ_{max}	ψ_{min} (Reference [3])	ψ_{max} (Reference [3])
A1	0	10^2	0	-2.272×10^{-1}	7.921×10^{-6}	-2.172×10^{-1}	4.063×10^{-6}
A2	0	10^3	0	-4.979×10^{0}	7.311×10^{-5}	-4.994×10^{0}	1.826×10^{-5}
A3 (200)	0	10^4	0	-4.047×10^{1}	2.413×10^{-1}	-4.117×10^{1}	1.044×10^{-1}
B1	0	10^2	-25	-4.785×10^{-2}	1.140×10^{-1}	-4.433×10^{-2}	1.177×10^{-1}
B2	0	10^3	-250	-1.491×10^{0}	1.084×10^{0}	-1.478×10^{0}	1.148×10^{0}
B3 (250)	0	10^4	-2500	-8.226×10^{0}	5.075×10^{0}	-8.725×10^{0}	5.388×10^{0}
C1	10^5	0	0	-1.213×10^{-3}	2.863×10^{1}	-5.798×10^{-4}	2.841×10^{1}
C2 (150)	10^6	0	0	-3.805×10^{-1}	9.320×10^{1}	-1.200×10^{-1}	9.251×10^{1}
D1	10^5	10^1	0	-1.178×10^{-3}	2.863×10^{1}	-5.785×10^{-4}	2.841×10^{1}
D2	10^5	10^2	0	-1.564×10^{-4}	2.860×10^{1}	-4.517×10^{-4}	2.838×10^{1}
D3	10^5	10^3	0	-5.562×10^{-1}	2.528×10^{1}	-5.677×10^{-1}	2.517×10^{1}

DOI: 10.1002/fld

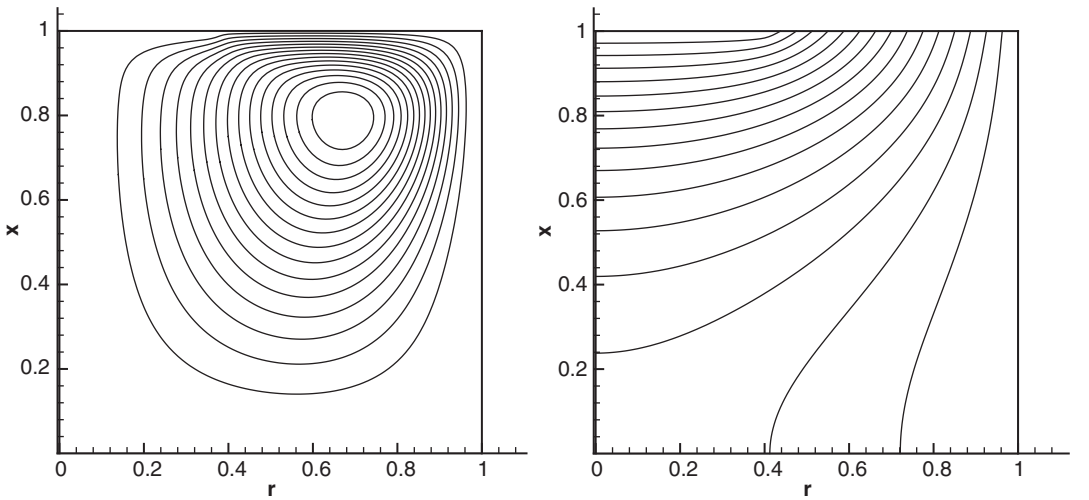

Figure 5. Streamlines and temperature contours of case A2, $Gr = 0$, $Re_x = 10^3$, $Re_c = 0$.

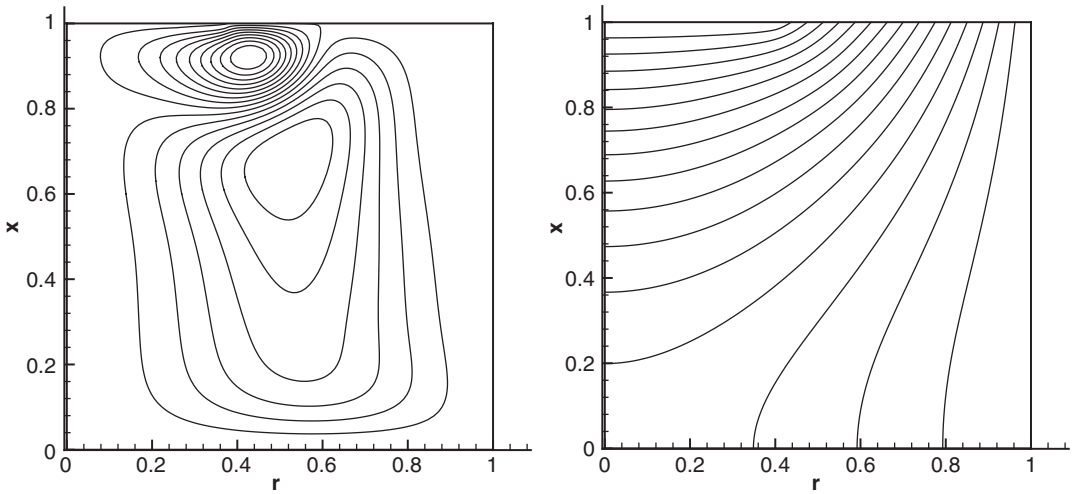

Figure 6. Streamlines and temperature contours of case B2, $Gr = 0$, $Re_x = 10^3$, $Re_c = -250$.

4.3. Numerical stability comparison

The numerical stability of LBM depends on the relax time τ, the Mach number of the flow and the size of mesh. It is well known that in LBM if τ is very close to 0.5, numerical instability would appear. $\tau_{\min}$ is usually case dependent. The Reynolds number is usually defined as

$$Re = \frac{UD}{v} = \frac{Uc(D/\delta_x)}{c_s^2(\tau - 0.5)}$$

DOI: 10.1002/fld

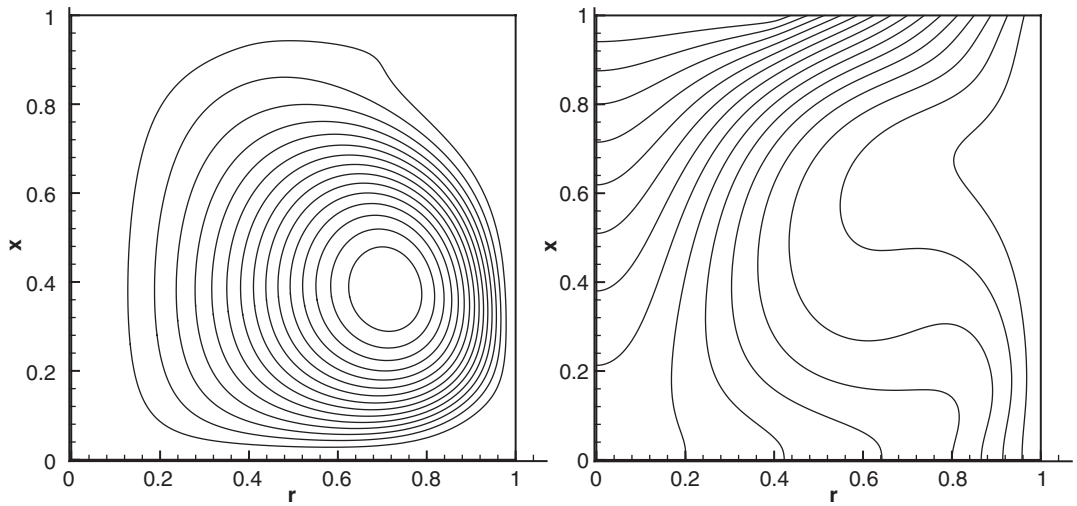

Figure 7. Streamlines and temperature contours of case C2, $Gr = 10^6$, $Re_x = 0$, $Re_c = 0$.

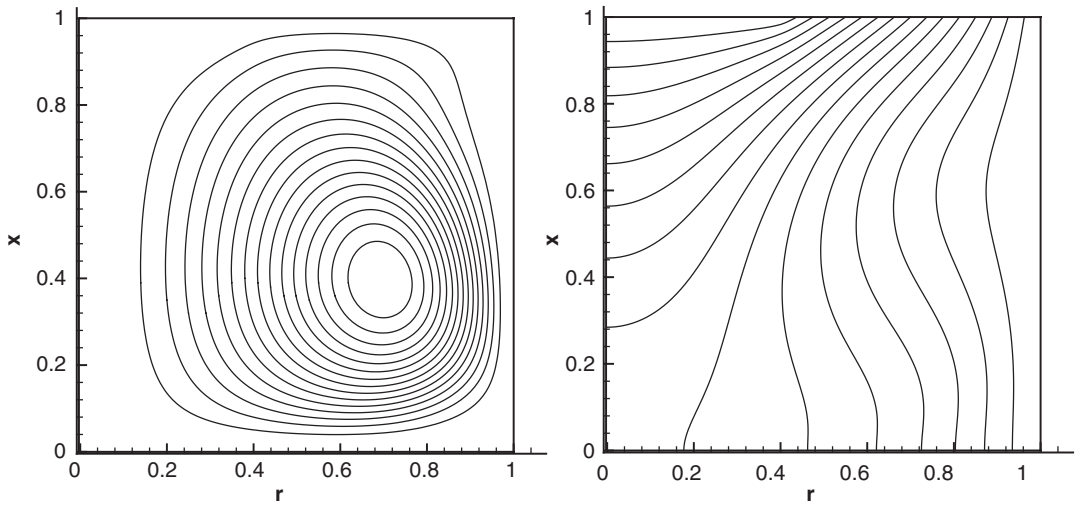

Figure 8. Streamlines and temperature contours of case D2, $Gr = 10^5$, $Re_x = 10^2$, $Re_c = 0$.

the Mach number in LBM is $U/c_s \ll 1$. To simulate cases of high Reynolds number, with limitation of τ_{min} and Mach number, usually we have to increase the value of (D/δ_x) (i.e. enlarge the grid size).

Generally speaking, adding complex position and time-dependent source terms into the LBE would decrease the numerical stability [15]. Compared with the previous axisymmetric D2Q9 model [5], the expression of the source terms $h_i^{(1)}$ and $h_i^{(2)}$ in present model are much simpler since the swirl velocity only appears in the term $h_i^{(2)}$. Hence, the present simpler model is expected to be more stable.

DOI: 10.1002/fld

Table V. Numerical stability comparison for case A1.

Grid	$\tau_{\min}$ (Present model)	$\tau_{\min}$ (Peng's model [5])
20×20	0.6125	0.6875
40×40	0.625	0.725
60×60	0.625	0.7375
80×80	0.625	0.7375
100×100	0.625	0.7375

To compare the numerical stability of our model and previous model [5], the benchmark case A1 of melt flow in CZ crystal growth was simulated by the two models with the same boundary condition treatment. As we know, the numerical stability can be demonstrated by the minimum τ value at which numerical instability does not appear. However, it is hard to find out the exact $\tau_{\min}$. But if the value of $\tau_{\min}$ is set as $\tau_{\min} = 0.5 + k * 0.0125$, where $k > 0$ is an integer, we may find out $\tau_{\min}$ roughly by finding the minimum k value at which numerical instability does not appear. So the numerical experiment was carried out to find $\tau_{\min}$. The $\tau_{\min}$ for the two axisymmetric D2Q9 models is listed in the Table V. From Table V, we can see that in all cases, $\tau_{\min}$ of present model are smaller than that of Peng *et al*. [5]. It seems our axisymmetric D2Q9 model is more stable.

The numerical stability is very important for simulation of high Reynolds number or high Grashof number cases. For example, if we want to simulate the case of $Gr = 10^7$, with the limitation of incompressible flow in LBM, U_t usually should not exceed 0.25, since $\nu = c_s^2 \delta_t (\tau - 0.5) = U_t R_c / \sqrt{Gr}$, if numerical stability requires $\tau \geqslant 0.6125$, then the mesh point in R_c should satisfy the relationship

$$\frac{R_c}{\delta_x} = \frac{c_s^2 (\tau - 0.5)\sqrt{Gr}}{c U_t} \geqslant \frac{1/3 \times (0.6125 - 0.5) \times \sqrt{10^7}}{1 \times 0.25} \approx 474$$

That means to simulate the case of $Gr = 10^7$, the coarsest grid should be 474×474, otherwise, the numerical instability would encounter in the simulation. While for the case of $Gr = 10^7$, if numerical stability of the Peng's model [5] requires $\tau \geqslant 0.7375$, grid as fine as 1000×1000 is required. Hence, our numerical method provides a significant advantage in simulation melt flow cases with high Reynolds number and high Grashof number.

5. CONCLUSION

As conventional CFD solvers, present hybrid scheme combining the LBMs and finite-difference method can solve the axisymmetric swirling flow as a quasi-3D problem. An axisymmetric incompressible lattice Boltzmann D2Q9 model was proposed in this paper by introducing an additional source term to LBE. With limit of Mach number $M \ll 1$ and $L_x/(c_s T) \ll 1$, this axisymmetric D2Q9 model successfully recovered the continuity equation and momentum equations for axial and radial velocities through Chapman–Enskog expansion (Appendix A). The equation for swirl velocity and the heat equation were solved by finite-difference methods.

This hybrid scheme was successfully applied to simulate the Taylor–Couette flow between two concentric cylinders. It was found that the residual convergence behaviour of this hybrid scheme is similar to that of explicit FVM. It is found that compared with LBM + FD solver, FLUENT

DOI: 10.1002/fld

requires about 3.35 times larger CPU time per iteration. However, to reach the same convergence criterion, the CPU time taken by our LBM + FD solver and explicit FVM solver are of same order.

The hybrid scheme was also applied to simulate flows in CZ crystal growth. Compared with results in other literatures [3, 4], the hybrid scheme can give out very accurate results for benchmark problems. Present axisymmetric D2Q9 model also seems more stable than that of Peng *et al.* [5]. As a result, this scheme can give accurate results for high Reynolds number and high Grashof number cases with smaller grid size.

APPENDIX A: BRIEF CHAPMAN–ENSKOG DERIVATION OF THE AXISYMMETRIC D2Q9 MODEL

We consider the problems of the laminar axisymmetric swirling flow of an incompressible liquid with an axis in x direction. The continuity equation (1) and NS momentum equations (2) in the pseudo-Cartesian coordinates (x, r) would be recovered from our axisymmetric D2Q9 model through the Chapman–Enskog expansion.

Here an incompressible D2Q9 model is used to derive our axisymmetric model. The nine discrete velocities of our model are illustrated in Equation (4). In our derivation we adopt $\delta_x = \delta_t$. The evaluation equation to describe 2D flow in (x, r) pseudo-Cartesian coordinates is illustrated as Equation (5). In our derivation, the Einstein summation convention is used.

As we know, the strategy for incorporating source terms into the LBE can be applied for fluid problems in which an external or internal force is involved. Gravity can be modelled by inserting source terms with different forms into LBE [16]. To simulate the particle–fluid suspensions, the forcing term is expanded in a power series in the particle velocity [17]. The form of source term [17] was also used to derive a correct representation of the forcing term [18]. For the above derivation [16–18], since the external or internal forces are simple, source term h_i is only expanded to first-order and there is no $h_i^{(2)}$ term.

However, to model the spatial and time-dependent 'forces' in RHS of Equations (1) and (2), source term h_i would be much more complex and should be expanded to second-order as that illustrated in Equation (A2) [10]. It is noticed that the choice of following forms of $h_i^{(1)}$ and $h_i^{(2)}$ or that in Reference [10] is only one particular strategy to incorporate 'geometrical source terms' into the LBM. The other possible strategies to derive axisymmetric models are suggested in detail in Reference [15].

At the beginning, we adopt the following expansions [10, 12]:

$$f_i(x + e_{ix}, r + e_{ir}, t + 1) = \sum_{n=0}^{\infty} \frac{\varepsilon^n}{n!} D^n f_i(x, r, t) \tag{A1}$$

$$\begin{aligned} f_i &= f_i^{(0)} + \varepsilon f_i^{(1)} + \varepsilon^2 f_i^{(2)} + \cdots \\ \partial_t &= \varepsilon \partial_{1t} + \varepsilon^2 \partial_{2t} + \cdots \\ \partial_\beta &= \varepsilon \partial_{1\beta} \\ h_i &= \varepsilon h_i^{(1)} + \varepsilon^2 h_i^{(2)} + \cdots \end{aligned} \tag{A2}$$

where $\varepsilon = \delta_t$ and $D \equiv (\partial_t + \mathbf{e}_\beta \cdot \partial_\beta)$, $\beta = x, r$ and x_α, x_β means x or r.

DOI: 10.1002/fld

Retaining terms up to $O(\varepsilon^2)$ in Equations (A1) and (A2) and substituting into Equation (5) results in the following Equations (A3)–(A5)

$$O(\varepsilon^0) : (f_i^{(0)} - f_i^{\mathrm{eq}})/\tau = 0 \tag{A3}$$

$$O(\varepsilon^1) : (\partial_{1t} + e_{i\beta}\partial_{1\beta}) f_i^{(0)} + f_i^{(1)}/\tau - h_i^{(1)} = 0 \tag{A4}$$

$$O(\varepsilon^2) : \partial_{2t} f_i^{(0)} + \left(1 - \frac{1}{2\tau}\right)(\partial_{1t} + e_{i\beta}\partial_{1\beta}) f_i^{(1)} + \frac{1}{2}(\partial_{1t} + e_{i\beta}\partial_{1\beta}) h_i^{(1)} + \frac{1}{\tau} f_i^{(2)} - h_i^{(2)} = 0 \tag{A5}$$

The distribution function f_i is constrained by the following relationships:

$$\sum_{i=0}^{8} f_i^{(0)} = \frac{p}{c_s^2}, \quad \sum_{i=0}^{8} e_{i\alpha} f_i^{(0)} = \rho_0 u_\alpha \tag{A6}$$

$$\sum_{i=0}^{8} f_i^{(m)} = 0, \quad \sum_{i=0}^{8} \mathbf{e}_i f_i^{(m)} = 0 \quad \text{for } m > 0 \tag{A7}$$

With the properties of the tensor $E^{(n)} = \sum_\alpha e_{\alpha 1} e_{\alpha 2}, \ldots, e_{\alpha n}$ [19], we have

$$\sum_{i=0}^{8} e_{i\alpha} e_{i\beta} f_i^{(0)} = \rho_0 u_\alpha u_\beta + p\delta_{\alpha\beta} \tag{A8}$$

$$\sum_i e_{i\alpha} e_{i\beta} e_{ik} f_i^{(0)} = \rho_0 c_s^2 (\delta_{jk}\delta_{\beta\alpha} + \delta_{j\alpha}\delta_{\beta k} + \delta_{j\beta}\delta_{\alpha k}) u_j \tag{A9}$$

Mass conservation and $h_i^{(1)}$

Summing on i in Equation (A4), we obtain at $O(\varepsilon)$

$$\partial_{1t}(p/c_s^2) + \rho_0 \partial_\beta u_\beta = \sum_i h_i^{(1)} \tag{A10}$$

which motivates the following selection of $h_i^{(1)}$ when comparing with the target dynamics of Equations (1) and (2). Rewriting (A10) in a dimensionless form, we can see that a condition of $L_x/(c_s T) \ll 1$ should be satisfied to neglect the first LHS term [12], where L_x is the character length in x direction, T is the character time of unsteady flow. That is an additional limit of our derivation besides condition Mach number $M \ll 1$.

To recover the continuity Equation (1), because $\sum_i \omega_i = 1$, the following selection of $h_i^{(1)}$ is reasonable [10]:

$$h_i^{(1)} = -\omega_i \rho_0 u_r / r \tag{A11}$$

Then we proceed to $O(\varepsilon^2)$ now. Summing on i in Equation (A5) gives

$$\partial_{2t}(p/c_s^2) + \sum_i \frac{1}{2}(\partial_{1t} + e_{i\beta}\partial_{1\beta}) h_i^{(1)} - \sum_i h_i^{(2)} = 0 \tag{A12}$$

DOI: 10.1002/fld

Since $\partial_{2t}(p/c_s^2)=0$ [12] and with our target dynamics in view, the remaining terms in Equation (A12) should vanish. Hence, we obtain

$$\sum_i h_i^{(2)} = \frac{1}{2}\sum_i (\partial_{1t} + e_{i\beta}\partial_{1\beta})h_i^{(1)} = \frac{1}{2}\left[\partial_{1t}\sum_i \left(\frac{-\omega_i \rho_0 u_r}{r}\right)\right] = -\frac{1}{2}\partial_{1t}\left(\frac{\rho_0 u_r}{r}\right) \tag{A13}$$

In the above process, we have used the results of $\sum_i \omega_i e_{i\beta}=0$.

Momentum conservation and $h_i^{(2)}$

Multiplying Equation (A4) by $e_{i\alpha}$ and summing on i, gives

$$\rho_0\partial_{1t}u_\alpha + \partial_{1\beta}\Pi^0_{\alpha\beta} = \sum_i h_i^{(1)} e_{i\alpha} = 0 \tag{A14}$$

where $\Pi^0_{\alpha\beta} = \sum_{i=0}^{8} e_{i\alpha}e_{i\beta}f_i^{(0)}$ is the zeroth-order momentum flux tensor. With $\Pi^0_{\alpha\beta}$ given by Equation (A8), Equation (A14) gives

$$\rho_0\partial_{1t}u_r = -\partial_\beta \Pi^0_{r\beta} = -\partial_\beta(p\delta_{r\beta} + \rho_0 u_\beta u_r) \tag{A15}$$

Substituting Equation (A15) into Equation (A13), we have a condition on the $h_i^{(2)}$

$$\sum_i h_i^{(2)} = \frac{1}{2r}\partial_\beta(p\delta_{r\beta} + \rho_0 u_\beta u_r) \tag{A16}$$

Multiplying Equation (A5) with $e_{i\alpha}$ and summing over i gives

$$\rho_0\partial_{2t}u_\alpha + \left(1-\frac{1}{2\tau}\right)\partial_{1\beta}\Pi^{(1)}_{\alpha\beta} = -\frac{1}{2}\left(\partial_{1t}\sum_i e_{i\alpha}h_i^{(1)} + \partial_{1\beta}\sum_i e_{i\alpha}e_{i\beta}h_i^{(1)}\right) + \sum_i h_i^{(2)}e_{i\alpha} \tag{A17}$$

where $\Pi^{(1)}_{\alpha\beta} = \sum_i e_{i\alpha}e_{i\beta}f_i^{(1)}$ is the first-order momentum flux tensor. With the aid of Equations (A4) and (A9), we have

$$\begin{aligned}
\Pi^{(1)}_{\alpha\beta} &= \sum_i e_{i\alpha}e_{i\beta}f_i^{(1)} = -\tau\sum_i e_{i\alpha}e_{i\beta}D_{1t}f_i^{(0)} + \tau\sum_i e_{i\alpha}e_{i\beta}h_i^{(1)} \\
&= -\tau\left[\partial_{1t}\Pi^{(0)}_{\alpha\beta} + \partial_k\left(\sum_i e_{i\alpha}e_{i\beta}e_{ik}f_i^{(0)}\right)\right] + \tau\sum_i e_{i\alpha}e_{i\beta}h_i^{(1)} \\
&= -\tau[\partial_{1t}\Pi^{(0)}_{\alpha\beta} + \rho_0 c_s^2(\delta_{\alpha\beta}\partial_j u_j + \partial_\beta u_\alpha + \partial_\alpha u_\beta)] - \rho_0\tau c_s^2\delta_{\alpha\beta}u_r/r
\end{aligned} \tag{A18}$$

For the first term in Equation (A18), using Equations (A10) and (A14) and the additional condition $L_x/(c_s T)\ll 1$, it is found that $\partial_{1t}\Pi^{(0)}_{\alpha\beta}$ are of $O(u^3)$. Hence, this term can be neglected [19]. Then, the second term in LHS of Equation (A17) can be written as

$$\begin{aligned}
\left(1-\frac{1}{2\tau}\right)\partial_{1\beta}\Pi^{(1)}_{\alpha\beta} &= -\tau\left(1-\frac{1}{2\tau}\right)\rho_0 c_s^2\left[\partial_{1\beta}\left(\delta_{\alpha\beta}\partial_j u_j + \frac{\partial u_\alpha}{\partial x_\beta} + \frac{\partial u_\beta}{\partial x_\alpha}\right) + \partial_{1\beta}(\delta_{\alpha\beta}u_r/r)\right] \\
&= -\nu\rho_0\partial_{1\beta}(\partial_\beta u_\alpha + \partial_\alpha u_\beta)
\end{aligned} \tag{A19}$$

DOI: 10.1002/fld

Substituting Equation (A19) into Equation (A17) and using the result of $\sum_i e_{i\alpha}e_{i\beta}h_i^{(1)} = c_s^2\delta_{\alpha\beta}\rho_0 u_r/r$, Equation (A17) can be written as

$$\frac{\partial u_\alpha}{\partial t} + \frac{\partial u_\beta u_\alpha}{\partial x_\beta} + \frac{\partial p}{\rho_0 \partial x_\alpha} - \nu\frac{\partial^2 u_\alpha}{\partial x_\beta^2} = \frac{1}{2}c_s^2\partial_\alpha\left(\frac{u_r}{r}\right) + \nu\partial_\alpha(\partial_\beta u_\beta) + \sum_i \frac{h_i^{(2)}}{\rho_0}e_{i\alpha} \tag{A20}$$

The RHS of (A20) can be written as

$$c_s^2(1-\tau)\partial_\alpha\left(\frac{u_r}{r}\right) + \sum_i \frac{h_i^{(2)}}{\rho_0}e_{i\alpha}$$

Comparing momentum Equation (A20) with Equation (2), to recover the NS momentum equations of axial and radial velocities, Equation (A21) should be satisfied

$$c_s^2(1-\tau)\partial_\alpha\left(\frac{u_r}{r}\right) + \sum_i \frac{h_i^2}{\rho_0}e_{i\alpha} = -\frac{u_\alpha u_r}{r} + \frac{\nu}{r}\left(\partial_r u_\alpha - \frac{u_r}{r}\delta_{r\alpha}\right) + \frac{u_z^2}{r}\delta_{\alpha r} + S \tag{A21}$$

Solving equation system of Equations (A16) and (A21), we can obtain the expression of $h_i^{(2)}$ as follows

$$\begin{aligned}\frac{h_i^{(2)}}{\rho_0} = {} & \frac{\omega_i}{2r}\left[\partial_\beta\left(\frac{p\delta_{r\beta}}{\rho_0} + u_\beta u_r\right)\right] + 3\omega_i\left[\frac{\nu}{r}\left(e_{i\beta}\partial_r u_\beta - \frac{u_r}{r}e_{ir}\right) - \frac{u_\beta u_r}{r}e_{i\beta}\right] \\ & - \omega_i(1-\tau)\partial_\beta\left(\frac{u_r}{r}\right)e_{i\beta} + 3\omega_i\left(\frac{u_z^2}{r}e_{ir} + \frac{e_{i\beta}S}{\delta_{\alpha\beta}}\right)\end{aligned} \tag{A22}$$

Equation (A22) can be rewritten explicitly as

$$\begin{aligned}\frac{h_i^{(2)}}{\rho_0} = {} & \frac{\omega_i}{2r}\left[\partial_r\left(\frac{p}{\rho_0}\right) + \partial_x u_x u_r + \partial_r u_r u_r\right] + \frac{3\omega_i\nu}{r}\left(\partial_r u_x e_{ix} + \partial_r u_r e_{ir} - \frac{u_r e_{ir}}{r}\right) \\ & - 3\omega_i\frac{u_r}{r}(u_x e_{ix} + u_r e_{ir}) - \omega_i(1-\tau)\left(\frac{\partial_x u_r}{r}e_{ix} - \frac{u_r}{r^2}e_{ir} + \frac{\partial_r u_r}{r}e_{ir}\right) \\ & + 3\omega_i\left(\frac{u_z^2}{r}e_{ir} + \frac{e_{ix}S}{\delta_{\alpha x}} + \frac{e_{ir}S}{\delta_{\alpha r}}\right)\end{aligned} \tag{A23}$$

The expression of $h_i^{(1)}$ [Equation (A11)], $h_i^{(2)}$ [Equation (A23)] are successfully derived and the continuity equation (1) and NS equation (2) can be fully recovered.

REFERENCES

1. Liu Y. Numerical simulation of flows in Czochralski crystal growth and Taylor vortices. *M. Eng. Thesis*, National University of Singapore, 1998.
2. Buckle U, Schafer M. Benchmark results for the numerical simulation of flow in Czochralski crystal growth. *Journal of Crystal Growth* 1993; **126**(4):682–694.

DOI: 10.1002/fld

3. Xu D, Shu C, Khoo BC. Numerical simulation of flows in Czochralski crystal growth by second-order upwind QUICK scheme. *Journal of Crystal Growth* 1997; **173**(1–2):123–131.
4. Raspo I, Ouazzani J, Peyret R. A spectral multidomain technique for the computation of the Czochralski melt configuration. *International Journal of Numerical Methods for Heat and Fluid Flow* 1996; **6**(1):31–58.
5. Peng Y, Shu C, Chew YT, Qiu J. Numerical investigation of flows in Czochralski crystal growth by an axisymmetric lattice Boltzmann method. *Journal of Computational Physics* 2003; **186**(1):295–307.
6. McNamara G, Zanetti G. Use of the Boltzmann equation to simulate lattice-gas automata. *Physical Review Letters* 1998; **61**(20):2332–2335.
7. Higuera F, Jimenez J. Boltzmann approach to lattice gas simulations. *Europhysics Letters* 1989; **9**(7):663–668.
8. Lee TS, Huang H, Shu C. An axisymmetric incompressible Lattice-BGK model for simulation of the pulsatile flow in a circular pipe. *International Journal for Numerical Methods in Fluids* 2005; **49**(1):99–116.
9. Huang H, Lee TS, Shu C. Lattice-BGK simulation of steady flow through vascular tubes with double constrictions. *International Journal of Numerical Methods for Heat and Fluid Flow* 2006; **16**(2):185–203.
10. Halliday I, Hammond LA, Care CM, Good K, Stevens A. Lattice Boltzmann equation hydrodynamics. *Physical Review E* 2001; **64**(011208):1–8.
11. Hou S, Zou Q *et al*. Simulation of cavity flow by the lattice Boltzmann Method. *Journal of Computational Physics* 1995; **118**:329–347.
12. He X, Luo L. Lattice Boltzmann model for the incompressible Navier–Stokes equation. *Journal of Statistical Physics* 1997; **88**(3/4):927–944.
13. Guo Z, Zheng C, Shi B. An extrapolation method for boundary conditions in lattice Boltzmann method. *Physics of Fluids* 2002; **14**:2007–2010.
14. Wheeler AA. 4 test problems for the numerical simulation of flow in Czochralski crystal growth. *Journal of Crystal Growth* 1990; **102**(4):691–695.
15. Huang H. Axisymmetric and three-dimensional lattice Boltzmann models and their applications in fluid flows. *Ph.D. Thesis*, National University of Singapore, 2006.
16. Buick JM, Greated CA. Gravity in a lattice Boltzmann model. *Physical Review E* 2000; **61**:5307–5320.
17. Ladd AJC, Verberg R. Lattice Boltzmann simulations of particle–fluid suspensions. *Journal of Statistical Physics* 2001; **104**:1191–1251.
18. Guo Z, Zheng C, Shi B. Discrete lattice effects on the forcing term in the lattice Boltzmann method. *Physical Review E* 2002; **65**(046308):1–6.
19. Lee TS, Huang H, Shu C. An axisymmetric incompressible lattice Boltzmann model for pipe flow. *International Journal of Modern Physics C* 2006; **17**(5):645–661.

DOI: 10.1002/fld